Spitzer Spectral Observations of the Deep Impact Ejecta

C. M. Lisse,[1,2]* J. VanCleve,[3] A. C. Adams,[3] M. F. A'Hearn,[2] Y. R. Fernández,[4] T. L. Farnham,[2] L. Armus,[5] C. J. Grillmair,[5] J. Ingalls,[5] M. J. S. Belton,[6] O. Groussin,[2] L. A. McFadden,[2] K. J. Meech,[7] P. H. Schultz,[8] B. C. Clark,[9] L. M. Feaga,[2] J. M. Sunshine[2]

Spitzer Space Telescope imaging spectrometer observations of comet 9P/Tempel 1 during the Deep Impact encounter returned detailed, highly structured, 5- to 35-micrometer spectra of the ejecta. Emission signatures due to amorphous and crystalline silicates, amorphous carbon, carbonates, phyllosilicates, polycyclic aromatic hydrocarbons, water gas and ice, and sulfides were found. Good agreement is seen between the ejecta spectra and the material emitted from comet C/1995 O1 (Hale-Bopp) and the circumstellar material around the young stellar object HD100546. The atomic abundance of the observed material is consistent with solar and C1 chondritic abundances, and the dust-to-gas ratio was determined to be greater than or equal to 1.3. The presence of the observed mix of materials requires efficient methods of annealing amorphous silicates and mixing of high- and low-temperature phases over large distances in the early protosolar nebula.

Before 2005, the best understanding we had of a comet's nucleus was obtained by studying the material emitted from the surface into the surrounding gravitationally unbound atmosphere (the coma). This understanding of the solar system's most primitive bodies, however, assumed that the information obtained from the coma could be extrapolated back to the surface and subsurface regions of the nucleus. There is now increasing evidence that comets evolve from their initial state, because of the effects of solar insolation, until their surfaces become devolatilized, hiding the pristine solar system material under a processed surface layer.

On 4 July 2005, NASA's Discovery mission Deep Impact (hereafter DI) sent a 364-kg impactor into the nucleus of comet 9P/Tempel 1 (hereafter Tempel 1) at 10.2 km s^{-1}. The impactor burrowed below the processed surface layers of the nucleus, releasing copious amounts of subsurface material in a prominent ejecta cone (1). The vast majority of the $\sim 10^6$ kg of material released in the impact [see the supporting online material (SOM)] was removed from the comet in an extremely gentle fashion, at low overpressures (<1 kPa) (2, 3) and temperatures,

thereby preserving the mineralogical nature of the component material at the micrometer-scale level, although deaggregation of large (>100 µm) fractal particles clearly occurred.

Here we describe Spitzer Space Telescope (SST) (4) infrared measurements of the solid materials excavated from the comet at the impact site. We used the highly sensitive Infrared Spectrograph (IRS) low-resolution ($R \sim 100$) modules of the SST (5, 6), obtaining four 60-s spectra over 5.2 to 14.5 µm and eight 30-s spectra over 14.0 to 38.0 µm at each pointing during the period from 2 to 5 July 2005. Basic data processing was performed using the IRS pipeline at the Spitzer Science Center (version S11.5). One-dimensional sky-subtracted spectra were extracted from these products, as described in (7). IRS peak-up (PU) images, used to center the comet in the 10″-wide spectrometer slit, were also used to obtain imaging photometry of the comet in a passband from 13 to 18.5 µm. At each pointing (Table 1),

we obtained two 16-µm PU images before obtaining spectra, allowing us to monitor the development of the impact ejecta (7).

Imaging observations. Pre-impact mid-infrared (IR) (16-µm) comet images obtained with the SST IRS peakup camera showed a normally active comet streaming dust from its nucleus into interplanetary space (Fig. 1, first panel). The dust seemed typical as compared to that seen in previous apparitions (8). About the size of fine sand (particles with an effective radius of 10 to 100 µm), it initially flows into space in all directions but then gets pushed back by the pressure of the Sun's light into the comet's tail.

After impact [05:52 universal time (UT), 4 July 2005], things changed dramatically (Fig. 1, right four panels). A stream of material was seen to flow outward from the nucleus toward the SW, in the downrange direction of the impact. A concomitant change was also seen in the SST PU light curves. In a 10″ × 10″ aperture, the 16-µm brightness of the comet's continuum shows a sharp, doubly inflected rise to a total excess of 25%. Similarly, a 5- to 35-µm spectrum of the comet taken 45 min after impact shows a flux density of about 5 janskys (Jy), 25% higher than the pre-impact coma signal of about 4 Jy. At the same time, the DI spacecraft observed a huge fog of fine particles with high optical depth and an abundance of dust so large that it completely obscured the impact site (1). The ejecta spectral signatures were detected from the time of impact through at least 41 hours afterward, but by 121 hours after impact, all spectral signatures above the pre-impact levels were absent.

Spectral observations. Using 5- to 35-µm time-resolved IRS spectra, we searched for the signature of fresh new subsurface dust in the 8- to 13-µm and 18-µm silicate emission bands, and their change as a function of time from pre-impact quiescence, through crater excavation, to post-impact active emission. From Infrared Astronomy Satellite (IRAS) observations of Tempel 1

[1]Planetary Exploration Group, Space Department, Johns Hopkins University Applied Physics Laboratory, 11100 Johns Hopkins Road, Laurel, MD 20723, USA. [2]Department of Astronomy, University of Maryland, CSS 2341, College Park, MD 20742, USA. [3]Ball Aerospace and Technologies Corporation, 1600 Commerce Street, Boulder, CO 80306, USA. [4]Department of Physics, University of Central Florida, Post Office Box 162385, Orlando, FL 32816–2385, USA. [5]Spitzer Space Science Center, California Institute of Technology, Pasadena, CA 91125, USA. [6]Belton Space Exploration Initiatives, 430 Randolph Way, Tucson, AZ, 85716, USA. [7]Institute for Astronomy, University of Hawaii, 2680 Woodlawn Drive, Honolulu, HI 96822, USA. [8]Department of Geological Sciences, Brown University, Providence, RI 02912–1846, USA. [9]Space Exploration Systems, Lockheed Martin, Denver, CO 80201, USA.

*To whom correspondence should be addressed.

Table 1. SST observations at I − 2 days to I + 2 days, with 5- to 35-µm spectroscopy and 2″ imaging at 16 µm. All observations are four-slit IRS low-resolution + PU imaging except for pointing no. 3, which is in the special high–time-resolution Instrument Engineering Request (IER) mode. Schedule calculations assume a heliocentric distance = 1.51 AU; an SST-to-comet distance = 0.75 AU; a 41-hour nucleus rotation period; an encounter time of 4 July 2005 06:00 UT; and a start time of observation −0.6 hours before the midpoint of observation, except for pointing no. 4, which is the long-duration (4.7 hours) IRS four-order observation with continual cycling between orders.

Pointing no.	Time since impact of pointing/length of pointing	No. of nucleus rotations since impact	Observation start time	Ground-based contemporaneous imaging site
1	−41.00 hours/1.18 hours	−1.00	2 July 12:23	–
2	−22.55 hours/1.18 hours	−0.55	3 July 06:50	Hawaii
3	−0.08 hour/0.55 hour	0.00	4 July 05:47	Hawaii
4	0.50 hour/4.7 hours (four complete spectra)	0.012	4 July 06:20	Hawaii
5	10.25 hours/1.18 hours	0.25	4 July 15:39	–
6	20.50 hours/1.18 hours	0.50	5 July 01:54	Chile
7	41.82 hours/1.18 hours	1.02	5 July 23:13	Chile

in 1983 (8), we expected a relatively featureless continuum before impact, with little silicate emission feature strength or deviation from local thermal equilibrium (LTE) blackbody behavior. This is because of the predominance of large dust particles in the natural coma emission, typical of other low-activity short-period comets. The SST pre-impact spectra revealed this near-LTE behavior with a color temperature of ~235 K (Fig. 2).

The immediate post-impact spectra showed a remarkable change in the outflowing material, with at least 16 strong spectral features, varying in strength from 20 to 140% of the ambient signal. The features directly correlate with those seen in the Infrared Space Observatory (ISO) spectrum of the extraordinarily active comet C/1995 O1 (Hale-Bopp) (Fig. 2) (9, 10) and those found in the spectrum of the very young stellar object (YSO) HD100546 (11).

Modeling and interpretation of the spectra. The spectra for the first 10 hours showed near-identical structure. Thus we focus here on the observations made during the first four pointings: the three taken before impact and the one taken at impact (I) + 30 to I + 60 min after impact. After isolating the ejecta emission from the normal coma and nucleus emission by subtracting the pre-impact spectrum, and removing the instrument artifacts and gross temperature effects by dividing the result by the pre-impact spectrum scaled to the best-fit ejecta continuum temperature (SOM), we found the emissivity spectrum of Fig. 3. Some strong characteristic emission features stand out immediately: carbonates at 6.5 to 7.2 μm, pyroxenes at 8 to 10 μm, olivines at 11 μm, and sulfides at 27 to 29 μm.

Next, the observed emissivity spectrum was compared to a linear combination of emission spectra of over 80 candidate mineral species, selected for their reported presence in YSOs, solar system bodies, dusty disk systems, and interplanetary dust particles (IDPs). When doing this comparison, the detailed properties of the ejected dust—the particle composition, size distribution, temperature, and porosity—all had to be addressed, because they can strongly affect the observed infrared flux. An accurate, thorough treatment without arbitrary simplifying assumptions is critical to the accuracy of our findings, and we describe our methodology at length in the SOM.

What is presented here are the results from a minimalistic model of the majority ejecta species, built from the fewest and simplest components possible. We do not claim to have found the exact mineral species with our technique; rather, we claim to have found the important mineral classes present in the ejecta and their gross atomic abundance ratios. A set of components was tested exhaustively before the addition of a new species was allowed, and only species that dropped the reduced chi-squared value χ^2_ν below the 95% confidence limit (CL) were kept. Current compositional models of cometary dust [such as the five-component model of Malfait et al. (11) and the three-component mixture of Harker et al. (12)] were tested, and none of them resulted in an acceptable fit at the 95% confidence level—more components were required. It is important to emphasize that although the number of parameters [composition, temperature, and particle size distribution (PSD)] may seem large, there were actually very few detected species for the 334 independent spectral points and 16 strong

features obtained at high signal-to-noise ratio by the SST/IRS over the 5- to 35-μm range. It was, in fact, extremely difficult to fit the observed spectrum within the 95% CL of $\chi^2_\nu = 1.13$.

The best-fit model reveals a spectrum dominated by compositional signatures in different wavelength regimes: water ice and gas, carbonates, and polycyclic aromatic hydrocarbons (PAHs) at 5 to 8 μm; silicates at 8 to 11 μm; carbonates, silicates, and PAHs at 11 to 20 μm; silicates and phyllosilicates at 20 to 35 μm; and sulfides at 27 to 29 μm (Fig. 3). The derived compositional abundances from our best-fit dust model with $\chi^2_\nu = 1.05$ are given in Table 2 (13). For the best-fit model, the relative atomic abundance we found in the ejected dust is H:C:O:Si:Mg:Fe:S:Ca:Al = 15:0.53:11:1.0:0.88:0.74:0.28:0.054: ≤ 0.085 (for Si = 1.0). The Si:Mg:Fe:Ca:Al ratios are consistent with solar system abundances determined from the Sun and from C1 chondrites, giving us confidence in our solution (14, 15).
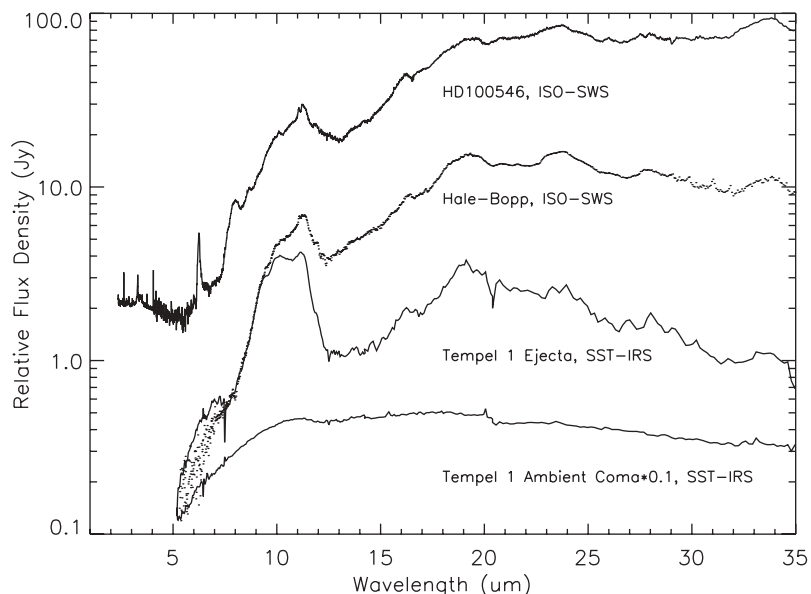

Fig. 2. SST 5- to 35-μm spectra of Tempel 1. From bottom to top, the traces are as follows: (i) spectrum of the ambient coma, taken 23 hours before impact; (ii) spectrum of the ejecta at I + 0.75 hours after impact; (iii) ISO spectrum of C/Hale-Bopp [after (9)]; (iv) ISO spectrum of YSO HD100546 [after (12)]. Note the logarithmic scale.

Fig. 1. IRS PU 16-μm imagery of the DI encounter. The first panel shows a total flux image of the comet, taken at I − 23 hours. There is appreciable signal throughout the field of view. The right four panels show the ratio of total flux image to the image at I − 23 hours. The green box shows the effective size of the IRS spectrometer entrance slit.
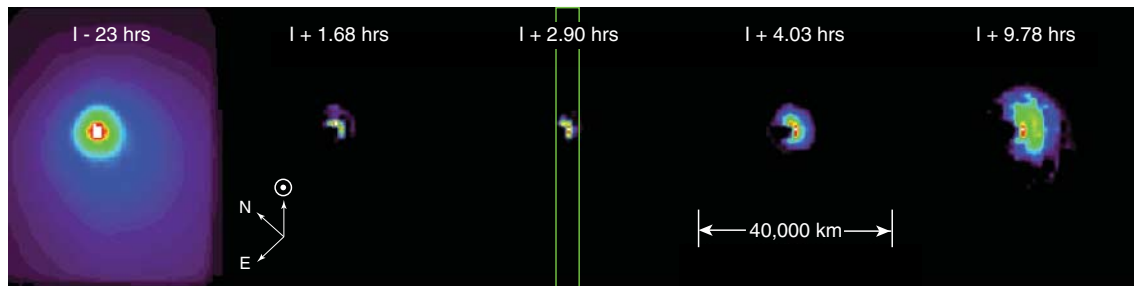
Compositional results. Here we discuss the 12 mineral species (plus PAHs and water ice and gas) found by our modeling, with emphasis on the plausibility of each detection and the constraints they place on the nature of the protosolar nebula (PSN).

Olivines. The dominant olivine species is Mg-rich forsterite, consistent with the results of numerous previous comet studies (16). New in our spectrum is a detection of fayalite, or Fe-rich olivine, in the ejecta. Some Fe is expected in the crystalline olivine component, as it is found in the amorphous olivine, but Nuth and Johnson (17) argue, however, that Fe may be preferentially in the amorphous silicates because the annealing of amorphous Fe-rich olivine into crystalline fayalite requires high temperature (~1400 K). Forsterite, on the other hand, requires annealing only at ~1100 K. Our results indicate that the crystalline forsterite:fayalite abundance ratio is 3.9 by mole fraction and that there is about half as much crystalline fayalite as total amorphous olivines. This suggests that the effective annealing temperature for the olivines incorporated into the comet was between 1100 and 1400 K and that the crystallization process was relatively efficient, because about 72% of the olivines are crystalline.

Pyroxenes. Tempel 1 was sufficiently bright after impact for the SST to detect the crystalline pyroxenes in the ejecta, and we found a pyroxene:olivine abundance ratio of about unity. In our spectrum, we found the majority of pyroxene as Fe-rich ferrosilite, with minority fractions of orthoenstatite and diopside. This suggests that much of the Fe that was not incorporated into Mg-rich olivines wound up instead in Fe-rich pyroxenes and sulfides. The mechanism for crystallizing the pyroxenes was almost complete: >90% of the pyroxenes were in crystalline form, which is consistent with the lower (versus olivines) pyrox-

ene annealing temperatures of 800 to 900 K. The presence of pyroxenes, both amorphous and crystalline, in comets was recently confirmed in comet Hale-Bopp (16).

Phyllosilicates. We found that ~8% of all silicates (by surface area) occurred in the form of phyllosilicates; the best match in our spectrum is the Fe-rich Na-bearing nontronite, a smectite-group mineral formed as an aqueous alteration product of basic rock. We did not find good fits with Mg-rich saponite or serpentine. The existence of hydrated silicates in comets is provocative, because it would suggest the presence of abundant amounts of reactive water in the formation region of the comet or in the cometary parent body. On the other hand, Brownlee (18) noted that there is a minority component of phyllosilicates in IDPs of likely cometary origin.

Smectite has a band near 2.35 μm, but no such feature has yet been reported in the DI spacecraft data. It was suggested as the cause of a near-IR feature seen in a spectrum of comet 124P/Mrkos (19). An absorption feature at that wavelength was also seen in a DS-1 spectrum of comet 19P/Borrelly's surface (20). The only major reservoir of Na in the observed dust was the notronite; it would be relatively labile upon dehydration and ultraviolet (UV) processing of the phyllosilicate, which is consistent with an extended dust source for the Na tails of comets (21).

Carbonates. In our SST spectrum (Figs. 2 and 3), there is a strong, broad, and persistent feature at 6.5 to 7.2 μm, arguing for a solid-state source. Carbonate species have a characteristic emission feature at these wavelengths. The carbonates magnesite (Mg-rich) and siderite (Fe-rich) fit the spectrum best; Ca-rich calcite and aragonite do not match the spectrum well. We also find the predicted secondary features at 11 to 12 μm and 13 to 14 μm in the data after removal of the silicate features (Fig. 4). The

amount of carbonates is about 5% of the total surface area of dust detected. The presence of carbonates is provocative because, like the phyllosilicates, liquid water was thought to be required to form carbonates from CO_2 in the presence of silicates. However, recent work by Toppani et al. (22) suggests that carbonates can be grown from the vapor phase in the presence of silicates, water, and carbon dioxide vapor.

Studies demonstrating the presence of carbonates in IDPs (23) suggest that our identification of cometary carbonates is plausible. Furthermore, Bradley (24) and Flynn et al. (25) have stated that in an analysis of their IDP sample libraries, carbonates and the 6.8-μm spectral feature are seen at the few-percent level in the anhydrous (cometary) IDPs. Reports of a (C, O, Mg) class of particles detected by the Giotto Particle Impact Analyzer (PIA) dust spectrometer during the 1P/Halley flyby in 1987 (26, 27) were interpreted as probably due to magnesite. Bregman et al. (28) observed comet 1P/Halley in 1987 with the Kuiper Airborne Observatory, detecting a transient 6.8-μm feature in one of the three resulting spectra.

PAHs. Using the PAH emission models of Li and Draine (29) for a mix of PAHs with average radius = 3 Å ($C_{14}H_{10}$) and standard deviation 1 Å, the spectral signature of PAHs at 6.2, 7.7, 8.6, and 11 μm was found in the I + 45 min spectra at the level of a few percent by total surface area [10^4 parts per million (ppm)] (Fig. 4). The emission line at 12.3 μm is much more subtle, because it is small compared to the strong silicate emission features at 8 to 12 μm. Confirmation of the PAH detection was provided by the hot PAH lines seen at 5.2, 5.8, 6.2, 7.7, and 8.2 μm in our high–time-resolution, transient SST spectra taken using an experimental mode (IER) of the IRS instrument during the first half hour after the impact.

Table 2. Composition of the best-fit model to the I + 45 min SST T1-DI ejecta spectrum. MW, molecular weight; N, number; T_{max}, maximum temperature.

Species	Weighted surface area	Density (g cm^{-3})	MW	N_{moles}* (relative)	Model T_{max} (°K)	Model χ^2_ν if not included
Amorphous olivine (MgFeSiO$_4$)	0.17	3.6	172	0.35	340	5.92
Forsterite (Mg$_2$SiO$_4$)	0.31	3.2	140	0.70	340	4.28
Fayalite (Fe$_2$SiO$_4$)	0.086	4.3	204	0.18	340	1.40
Amorphous pyroxene (MgFeSi$_2$O$_6$)	0.041	3.5	232	0.06	340	1.38
Ferrosilite (Fe$_2$Si$_2$O$_6$)	0.33	4.0	264	0.50	295	9.30
Diopside (CaMgSi$_2$O$_6$)	0.115	3.3	216	0.18	340	1.86
Orthoenstatite (Mg$_2$Si$_2$O$_6$)	0.10	3.2	200	0.16	340	1.70
Smectite notronite (Na$_{0.33}$Fe$_2$(Si,Al)$_4$O$_{10}$(OH)$_2$ * 3H$_2$O)	0.14	2.3	496	0.07	340	3.76
Magnesite (MgCO$_3$)	0.030	3.1	84	0.11	340	1.30
Siderite (FeCO$_3$)	0.051	3.9	116	0.17	340	1.83
Niningerite (Mg$_{50}$Fe$_{50}$S)	0.15	4.5	72	0.92	340	2.51
PAH (C$_{10}$H$_{14}$), ionized	0.039	1.0	<178>	0.022	N/A	1.58
Water ice (H$_2$O)	0.049	1.0	18	0.27	220	1.40
Water gas (H$_2$O)	0.028	1.0	18	23.7†	220	1.22
Amorphous carbon (C)	0.068	2.5	12	1.45	390	13.3

*N_{moles} ~ density/molecular weight × surface area weighting; ± 10% errors on the abundances (2σ).   †Determined using a g factor of 2.2 × 10^{-4}, normalization of 5.8 × 10^5 kg of total water gas, and 7.8 × 10^5 kg of total dust mass in the beam.

PAHs have been suspected to be cometary constituents since their detection in the interstellar medium (ISM) and in YSOs (30–32). To date, no direct detection of PAHs in comets has been made; the strongest claim was produced by Bockelee-Morvan et al. (33), who examined the 3.2- to 3.6-μm emission in seven comets, and by removing the known species, found a small residual near the 3.28-μm aromatic C–H stretch wavelength. The amount of PAHs suggested by the residual, however, was quite small, on the order of 1 ppm versus water.

The emitting characteristics of PAH molecules, triggered by the stochastic absorption of one UV photon, allow them to emit in the mid-IR even when "normal" dust grains in LTE do not emit appreciable flux. The relative strengths of the different PAH features depend on the molecules' size and charge state. Our best-fit model shows a clear preference for the ionized rather than neutral PAH signature, implying that the rate of PAH ionization is fast enough that the majority of PAHs are ionized within 45 min of exposure to sunlight at 1.5 astronomical units (AU).

Sulfides. It is clear that there are two emission peaks from 27 to 29 μm that are not due to silicates (Fig. 4). The Fe-S stretch feature is at ~30 μm, and the Mg-S stretch is at 25 to 40 μm; however, these features are highly dependent on the crystal structure and Mg/Fe stochiometry of the system (34–36). We can rule out crystalline troilite and pyrite as contributing significantly to the observed spectrum, as well as the more oxidized cognate sulfate species. On the other hand, the MgFeS ningerite fit could be improved, and nonstoichiometric pyrrohtite or pentlandite, as suggested by the preliminary STARDUST results, have features at 24.5 μm, consistent with one of the apparent (but noisy) peaks in our residuals. We conclude that the actual sulfide phase in the ejecta has yet to be properly identified; a problem similar to that faced by Hony et al. (37) in studying iron sulfides formed and ejected from carbon stars.

The presence of metal sulfides in cometary dust is plausible; iron sulfides are found in abundance in IDPs (38). Sulfur is half as abundant as Fe or Mg in the solar system but appears depleted in cold dense molecular clouds with embedded young stellar objects, indicating that most of it probably resides in solid grains. Schulze and Kissel (39) found strong evidence for Fe-rich sulfides from the PIA in situ measurements at comet 1P/Halley.

Water ice. Water ice is present in low but detectable quantities (3% by surface area) in the SST spectra, as a broad feature at 10.5 to 15 μm. The spectral signature of water ice is attenuated and reddened as compared to those of the other ejecta solids, because the ice is at much lower temperatures than the rest of the dust. Thus, the water ice spectral signature is subtle and required detailed modeling to detect the shoulder longward of the strong 8- to 12-μm silicate emission peak.

Detection of water ice was expected, because water is the major volatile species in comets, and Sunshine et al. (40), using the DI High Resolution Instrument (HRI)–IR spectrometer, demonstrated the presence of significant amounts of water ice in the ejecta at I + 14 min. The presence of fragile, labile water ice in the ejecta confirms the relative absence of processing by the DI collision. The mean icy grain particle temperature found from our fits, 220 K, is somewhat above the expected pure ice grain temperature controlled by sublimation, which argues that we were observing dirty, crystalline water ice grains.

Water gas. Water gas does not suffer from the thermal damping effect, and the broad, relatively strong H_2O v_2 out-of-plane molecular vibration is the source of the small but significant 6-μm emission feature seen in the SST data (41). The amount of water detected in the SST beam is $\sim 5.8 \times 10^5$ kg, assuming a g factor for the v_2 band of water at 6.27 μm of 2.2×10^{-4} s^{-1} (42). Compared with the minimum dust mass required by the Spitzer spectrum, 7.8×10^5 kg (table S1), this implies a dust/gas ratio of the ejecta of at least 1.3.

Amorphous carbon. The final constituent found in the comet consists of optically dark, highly absorbing particles of amorphous carbon. Abundant amorphous solid carbon is found in IDPs and is a well-known species in comets, and the presence of abundant carbon grains in the ISM has been inferred from the 2200 Å feature in the interstellar extinction law. It is this component, when fractionated into small individual pieces, that gives rise to the bulk of the "superheat," or positive deviation from LTE, at short wavelengths (3 to 8 μm) in cometary dust spectra. These particles are very hot, efficiently absorbing sunlight while poorly reemitting long-wavelength thermal radiation.

The total amount of carbonaceous material (carbonates, amorphous carbon, and PAHs) detected in our I + 45 min spectra is 20% of the amount of silicates found. "Typical" comets studied in our survey have abundances of 33 to 50%, so Tempel 1 seems to be somewhat depleted in carbonaceous material as compared with the typical comet; A'Hearn et al. (43), in their survey of 85 comets, found Tempel 1 to be typical, but near the low end of typical, in terms of its C_2 abundance (8).

PSN implications and parent-body evolution. From our results, comet Tempel 1 appears to contain high-temperature crystalline silicates formed by annealing at temperatures
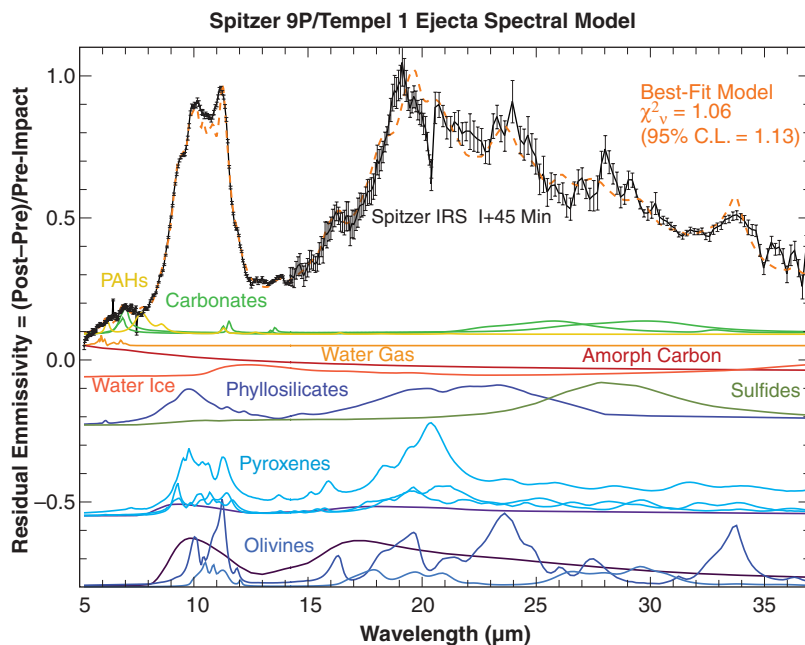

Fig. 3. Emissivity spectrum for the Tempel 1 ejecta, measured at I + 45 min. Silicates dominate the observed emission. The black line shows the SST ejecta spectrum, divided by the pre-impact spectrum normalized to a 235 K blackbody. Error bars are ±2σ. The orange dashed line shows the best-fit model spectrum. The colored curves show emission spectra for the constituent species, scaled by the ratio $B_\lambda[T_{dust}(a)_i]/B_\lambda(T_{post-impact})$, where the temperature T is for a particle or radius a and composition i, and $T_{post-impact}$ = 390 K is found from the best fit of a blackbody B_λ to the post-impact continuum. The best-fit model individual species curves have been scaled by a factor of 2 versus the data for emphasis. Dark purples, amorphous silicates of pyroxene or olivine composition. Light blues, crystalline pyroxenes: ferrosilite, diopside, and orthoenstatite, in order of 20-μm amplitude. Dark blues, crystalline olivines, forsterite, and fayalite, in order of 20-μm amplitude. Red, amorphous carbon. Deep orange, water ice. Light orange, water gas. Yellow, PAHs. Bright greens, carbonates: siderite and magnesite, by order of 7-μm emissivity amplitude. Olive green, sulfides, represented here by ningerite.

>1000 K, combined with mid-temperature phyllosilicates and sulfides formed at temperatures ~600 K, plus water ice, which is stable up to ~200 K, and highly volatile gas species such as CO, CO_2, and CH_4, present as ices, which are stable only at temperatures less than 100 K. The presence of such diverse species in the interior of comet 9P/Tempel 1 has important implications for the state of the PSN at the time of the comet's formation, ~4.5 billion years ago, and its evolutionary history since its formation.

PSN mixing. There is now strong evidence (44) that there must be a mechanism for crystallizing silicates in the PSN, because they come from the ISM as amorphous material. If this was done by thermal heating of material near the young Sun (temperatures >1000 K were reached only inside the present orbit of Mercury), then there must also have been a method for efficiently transporting the silicates out to the formation region of the comet. Tempel 1, a Jupiter family comet, was originally formed in the trans-neptunian region of the PSN, at its outer edges. The same mechanism may have been responsible for taking carbonates and phyllosilicates, formed in the regions of the PSN with abundant water vapor (0.5 to 3.0 AU), out to the region of cometary formation. The implication of strong mixing—that the cometary bodies should be relatively similar in composition to the bulk PSN—is consistent with the near-solar atomic abundances found from the SST spectra. (Another annealing mechanism, shock waves due to the formation of the giant planet cores or the young Sun's turbulence, is not consistent with the fluffy, porous, ISM-like aggregate dust found in the ejecta; it is more likely to create chondrule-like objects by total disruption of the local material, followed by recondensation. It is also not consistent with the high crystalline forsterite:fayalite ratio of 3.9:1 and the near 1:1 abundance of crystalline pyroxenes, which argues for a well-defined dust annealing temperature of no less than 900 K and no more than 1200 K.)

The PSN mixing cannot have been perfect, however, or else the solar system would be highly homogenous and asteroids would merely be comets with few to no volatiles. This is clearly not the observed case. Trends in compositional diversity are evident in the asteroid belt, with the most primitive asteroids being in the outer regions. The density, porosity, and tensile strength measurements from the DI mission for Tempel 1 are in disagreement with similar measurements for asteroids (45). A likely possibility is that the mixing occurred early on, in a relatively warm PSN, and then turned off, allowing sufficient time for significant small body evolution afterward. A natural time scale is the 5 million to 10 million years after nebula formation, when the giant planet cores formed and inhibited further radial transport across their orbits (46, 47). This would create a quantity of nebular crystalline silicates, phyllosilicates, and carbonates that was time-dependent, resulting in variability in the comet compositional spectrum (48).

Parent-body alteration. The ejecta material from comet Tempel 1 is a good representation of the material from which the comet was formed, unless changes have occurred in the parent body over 4.5 billion years. For example, the aqueous alteration suggested by the detection of phyllosilicates and carbonates could have been caused in two ways: suddenly, by producing abundant warm water during impacts, or slowly, by a thermal wave from the Sun penetrating into the depths of the comet and heating a boundary layer between the cold icy core and the warm gaseous coma at the nucleus surface.

The thermal layer mechanism would make a thin altered region all over the comet, wherever sublimation was occurring. Even though the DI experiment sampled material from only one location, the match between the Tempel 1 spectrum and the C/1995 O1 (Hale-Bopp) spectrum argues for a global mechanism: The material from Hale-Bopp was emitted from at least five strong jets, well spaced over the surface of the comet (49). The work of Sarid et al. (50) casts doubts on the intrinsic liquid water layer model; it is more likely that there are regions of strong water vapor flow. The impact mechanism would alter compositions in the vicinity of an impact site and has the advantage of providing high transient temperatures and pressures as well. The location of the DI impact site lay between two established impact craters, in a depression apparently excavated by the heating incurred during repeated perihelion passages of the comet (1). Consistent with this model, new laboratory work by Toppani et al. (22) has demonstrated the ability to grow carbonate crystals from hot silicate, water, and carbon dioxide vapors. However, there must be limits to this processing; it is difficult to understand how the material excavated by DI could have been impact-processed to the ~1200 K crystalline silicate annealing temperature indicated by the SST spectra, while at the same time retaining the low density, low tensile strength, high porosity, and evidence of volatile ices determined for the interior material by DI (1).

The match between the Tempel 1 ejecta spectrum (Fig. 2) and the HD100546 dusty disk spectrum argues for a similar origin of the comet and YSO material. Ceccarelli et al. (51) and Chiavassa et al. (52) have also found that half of all YSOs in the ISO Long Wavelength Spectrometer survey display emission due to carbonates. If parent-body processes are the origin of the altered species, then there must also be a mechanism for reemitting large amounts of the species into the surrounding nebula in significant quantities (such as jets or collisional fragmentation).

References and Notes

1. M. F. A'Hearn et al., Science **310**, 258 (2005).
2. D. Stoffler et al., J. Geophys. Res. **80**, 4062 (1975).
3. H. J. Melosh, in Impact Cratering: A Geologic Process (Oxford Monographs on Geology and Geophysics, No. 11, Clarendon Press, Oxford, 1989).
4. M. W. Werner et al., Astrophys. J. Suppl. **154**, 1 (2004).
5. J. R. Houck et al., Astrophys. J. Suppl. **154**, 18 (2004).
6. The SST is the most sensitive mid-infrared observing platform ever built, due to its location in a stable space environment orbit above the terrestrial atmosphere and to its operations at superfluid helium temperatures. The background level at 5 μm for the SST IRS was 6 orders of
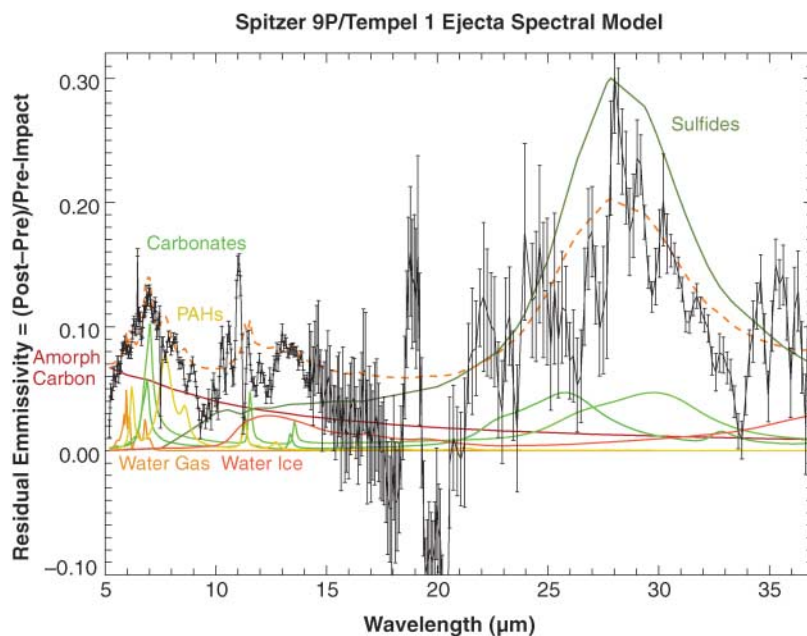
Fig. 4. Enhanced nonsilicate emissivity spectrum. Same as in Fig. 3, except with the silicate emission contributions removed. Left are the residual emission features due to PAHs, carbonates, amorphous carbon, water ice and gas, and sulfides. Error bars are 2σ. The best-fit model individual species curves have been scaled by a factor of 2 versus the data for emphasis. The large residual at 21 μm is due to problems with matching the spectra between the orders and slits.

magnitude less per pixel than for the DI HRI-IR passively cooled spectrometer, resulting in SST spectra taken at 0.75 AU from the comet with precisions rivaling those obtained by the HRI-IR, taken at 1000 km (6.8×10^{-6} AU) from the comet.

7. C. M. Lisse et al., Astrophys. J. Lett. **625**, L139 (2005a).
8. C. M. Lisse et al., Space Sci. Rev. **117**, 161 (2005b).
9. J. Crovisier. et al., Science **275**, 1904 (1997).
10. E. Lellouch et al., Astron. Astrophys. **339**, L9 (1998).
11. K. Malfait et al., Astron. Astrophys. **332**, L25 (1998).
12. D. E. Harker et al., Science **310**, 278 (2005).
13. As a test of the robustness of our best-fit model, the last column in Table 2 also gives the best-fitting χ^2_ν we could find if we deleted a particular species while keeping the rest.
14. E. Anders, N. Grevesse, Geochim. Cosmochim. Acta **53**, 197 (1989).
15. H is very deficient, as expected for small primitive bodies' inability to retain solar nebula H_2. C is deficient by a factor of 10, due to its majority partitioning into the comet's labile icy volatiles (CH_4, C_2H_6, CO, and CO_2). E. K. Jessberger et al. (53) found a C/Mg ratio (atom/atom) in 79 selected large particles during the flythrough of the coma of 1P/Halley that was an order of magnitude greater than in typical IPDs. O is less deficient than C, depleted by only a factor of ~2, due to its more lithophilic chemistry and majority presence in the relatively involatile H_2O. S appears deficient by a factor of 1.5, suggesting that we may not have well characterized the sulfide constituents or that a significant fraction of S was present in volatile species such as H_2S.
16. D. Wooden et al., Astrophys. J. **517**, 1034 (1999) and references therein.
17. J. A. Nuth, N. M. Johnson, Icarus **180**, 243 (2006).
18. D. Brownlee, personal communication.
19. J. Licandro et al., Astron. Astrophys. **398**, L45 (2003).
20. L. A. Soderblom et al., Icarus **167**, 100 (2004).
21. J. K. Wilson et al., Geophys. Res. Lett. **25**, 225 (1998).
22. A. Toppani et al., Nature **437**, 1121 (2005).
23. S. Sandford, Science **231**, 1540 (1986).
24. J. Bradley, personal communication.
25. G. J. Flynn et al., in Dust in Planetary Systems, proceedings of the conference held 26 to 28 September 2005, Kaua'i, Hawaii (Lunar and Planetary Institute Contribution No. 1280, 2005), p. 48.
26. B. C. Clark et al., Astron. Astrophys. **187**, 779 (1987).
27. Also reported by M. N. Fomenkova et al. (54), based on on the fact that F. K. Rietmeijer (55) had reported carbonates and layer silicates as minor phases in anhydrous chondritic porous IDPs.
28. J. D. Bregman et al., Astron. Astrophys. **187**, 616 (1987).
29. A. Li, B. T. Draine, Astrophys. J., in press.
30. K. Tomeoka, P. R. Buseck, Science **231**, 1544 (1986).
31. L. Deutsch et al., Astrophys. Space Sci. **224**, 89 (1995).
32. M. S. Hanner et al., Astrophys. J. **502**, 871 (1998).
33. D. Bockelee-Morvan et al., Icarus **116**, 18 (1995).
34. Y. Kimura et al., Astron. Astrophys. **442**, 507 (2005).
35. L. P. Keller et al., Nature **417**, 148 (2002).
36. L. P. Keller et al., Lunar Planet. Sci. Conf. **XXXI**, abstract 1860 (2000).
37. S. Hony et al., Astron. Astrophys. **393**, L103 (2002).
38. J. P. Bradley, in Astromineralogy, vol. 609 of Lecture Notes in Physics, T. Henning, Ed. (Springer-Verlag, Berlin-Heidelberg-New York, 2002), pp. 217–235.
39. H. Schulze, J. Kissel, Meteoritics **27**, 286 (1992).
40. J. S. Sunshine et al., Science **311**, 1453 (2006).
41. Due to an O-H bending mode, the broad 6.0-μm feature is similar to the broad 3-μm water ice absorption feature. It had not been positively detected in comets before DI, although Bregman et al. (28) allude to a "deficit versus the best fit greybody at 6.0 μm" in the December 1985 spectrum of comet 1P/Halley.
42. J. Crovisier, personal communication.
43. M. F. A'Hearn et al., Icarus **118**, 223 (1995).
44. C. Kemper et al., Astrophys. J. **609**, 826 (2004).
45. A. Cheng, Adv. Space. Res. **33**, 1558 (2004).
46. A. P. Boss, Astrophys. J. **616**, 1265 (2004).
47. H.-P. Gail, Astron. Astrophys. **413**, 571 (2004).
48. J. A. Nuth et al., Nature **406**, 275 (2000).
49. S. M. Lederer, H. Campins, Earth Moon Planets **90**, 381 (2002).
50. G. Sarid et al., Pub. Astron. Soc. Pacific **117**, 796 (2005).
51. C. Ceccarelli et al., Astron. Astrophys. **395**, L29 (2002).
52. A. Chiavassa et al., Astron. Astrophys. **432**, 547 (2005).
53. E. K. Jessberger et al., Nature **332**, 691 (1988).
54. M. N. Fomenkova et al., Science **258**, 266 (1992).
55. F. J. Rietmeijer, Earth Planet. Sci. Lett. **102**, 148 (1991).
56. This paper was based on observations taken with the NASA SST, operated by the Jet Propulsion Laboratory (JPL)/CalTech, under JPL contracts 1274400 and 1274485. The authors thank S. Bajt, J. Bradley, D. Brownlee, N. Chabot, B. Clark, N. Dello-Russo, G. Flynn, W. Glaccum, C. Grady, E. Gruen, D. Harker, K. Hibbits, W. Jackson, D. Joswiak, L. Keller, D. Lauretta, A. Li, J. Nuth, W. Reach, A. Rivkin, and D. Wellnitz for valuable discussions; G. Flynn and M. Sitko for their invaluable reviews; and J. Jackson and S. Kido for their help with the graphics.

Netrins Promote Developmental and Therapeutic Angiogenesis

Brent D. Wilson,[1,2]* Masaaki Ii,[7]*† Kye Won Park,[1,3]* Arminda Suli,[4]*
Lise K. Sorensen,[2] Frederic Larrieu-Lahargue,[1] Lisa D. Urness,[1,2] Wonhee Suh,[1]‡
Jun Asai,[7] Gerhardus A.H. Kock,[7]§ Tina Thorne,[7] Marcy Silver,[7] Kirk R. Thomas,[1,5]
Chi-Bin Chien,[4,6]∥ Douglas W. Losordo,[7]∥ Dean Y. Li[3]∥

Axonal guidance and vascular patterning share several guidance cues, including proteins in the netrin family. We demonstrate that netrins stimulate proliferation, migration, and tube formation of human endothelial cells in vitro and that this stimulation is independent of known netrin receptors. Suppression of *netrin1a* messenger RNA in zebrafish inhibits vascular sprouting, implying a proangiogenic role for netrins during vertebrate development. We also show that netrins accelerate neovascularization in an in vivo model of ischemia and that they reverse neuropathy and vasculopathy in a diabetic murine model. We propose that the attractive vascular and neural guidance functions of netrins offer a unique therapeutic potential.

Neuronal pathfinding is directed by a series of extracellular guidance cues that either attract or repulse growing axons. All of the four major families of neural guidance cues—ephrins, semaphorins, slits, and netrins—have been shown to direct patterning in the vascular system (1–4). The netrins are the prototypical axonal attractants, first identified as extracellular factors secreted from the floor plate that attract spinal commissural axons toward the midline (5). This family includes netrin-1, netrin-2 (netrin-3 in mouse), netrin-4, and the netrin-related molecules, netrin-G1 and netrin-G2.

The signaling pathways for netrin-1 are best understood. Receptors in the deleted in colorectal cancer (DCC) subfamily (DCC and neogenin) mediate axon attraction toward netrin-1 (2), although this signal can be converted from an attractive to a repulsive cue by binding of netrin to the Unc5b receptor (6). The adenosine 2b receptor (A2b) reportedly binds to netrin-1 (7), but its role in netrin-mediated axonal extension has been questioned (8).

Netrins have roles that extend beyond axonal guidance. The netrins are expressed in Schwann cells, are required for regeneration and maintenance of the central nervous system (9, 10), and have been implicated in the development of mammary gland, lung, pancreas, and blood vessel (11–14). Although others have reported that netrin-1 inhibits endothelial migration and blocks filopodial extension through the repulsive netrin receptor Unc5b (14), we have suggested that netrin-1 functions as a proangiogenic factor (13).

Netrins are endothelial mitogens and chemoattractants. To further elucidate the activity of netrins, we first evaluated the effects of purified netrin proteins on the behavior of human microvascular endothelial cells (HMVECs) in vitro. Netrin-1, -2, and -4 all stimulated migration of HMVECs in a dose-dependent fashion (Fig. 1), inconsistent with a published report concluding that netrin-1 inhibited migration of endothelial cells (14). To exclude the possibility of contamination in our netrin preparations, we used mass

[1]Program in Human Molecular Biology and Genetics, [2]Division of Cardiology, [3]Department of Oncological Sciences, [4]Department of Neurobiology and Anatomy, [5]Division of Hematology, [6]Brain Institute, University of Utah, Salt Lake City, UT 84112, USA. [7]Division of Cardiovascular Research, Caritas St. Elizabeth's Medical Center, Tufts University School of Medicine, Boston, MA 02135, USA.

*These authors contributed equally to this work.
†Present address: Stem Cell Translational Research, Institute of Biomedical Research and Innovation/RIKEN Center for Developmental Biology, Kobe 650-0047, Japan.
‡Present address: Department of Medicine, Samsung Medical Center, Samsung Biomedical Research Institute, Sungkyunkwan University School of Medicine, 50 Ilwon-dong, Kangnam-Ku, Seoul 135-710, Korea.
§Present address: Department of Cardiology, Thoraxcenter, University Medical Center Groningen, University Groningen, 30.001 Groningen, Netherlands.
∥To whom correspondence should be addressed. E-mail: dean.li@hmbg.utah.edu (D.Y.L.); douglas.losordo@tufts.edu (D.W.L.); chi-bin.chien@neuro.utah.edu (C.B.C)